Y_2Te_3: A New n-type Thermoelectric Material†

Michael Y. Toriyama,[a*] Dean Cheikh,[b] Sabah K. Bux,[b] G. Jeffrey Snyder,[a] Prashun Gorai[c*]

Rare-earth chalcogenides $Re_{3-x}Ch_4$ (Re = La, Pr, Nd, Ch = S, Se, Te) have been extensively studied as high-temperature thermoelectric (TE) materials owing to their low lattice thermal conductivity (κ_L) and tunable electron carrier concentration via cation vacancies. In this work, we introduce Y_2Te_3, a rare-earth chalcogenide with a rocksalt-like vacancy-ordered structure, as a promising n-type TE material. We computationally evaluate the intrinsic transport properties, optimized TE performance, and doping characteristics of Y_2Te_3. We find that Y_2Te_3 exhibits low κ_L in agreement with previous experiments. Combined with a large conduction band (CB) degeneracy, Y_2Te_3 has a high n-type TE quality factor. Interestingly, our electronic structure calculations reveal the presence of multiple low-lying conduction band valleys, which opens opportunities for further improvement of TE performance through band convergence. We use defect calculations to show that Y_2Te_3 is n-type dopable under Y-rich growth conditions, which suppresses the formation of acceptor-like cation vacancies. Furthermore, we propose that degenerate n-type doping can be achieved with halogens (Cl, Br, I), with I being the most effective dopant. Our computational results as well as experimental results reported elsewhere make the case for further optimization of Y_2Te_3 as a n-type TE material.

1 Introduction

The efficiency of a thermoelectric (TE) device largely depends on the dimensionless material figure of merit $zT = \alpha^2\sigma T/\kappa$, where α is the thermopower, σ is the electrical conductivity, κ is the thermal conductivity, and T is the temperature.[1] A route to achieving higher zT is through reduction of κ. Since materials with low κ are desired, many studies have been dedicated towards discovering novel low-κ materials for TE applications.[2–10] Zhu et al.[10] combined graph neural networks and random forest approaches to identify rare-earth chalcogenides e.g., Y_2Te_3 and Er_2Te_3, as materials with low lattice thermal conductivity (κ_L), in direct agreement with known high-performing TE materials.[11–13] $La_{3-x}Te_4$, which has been extensively studied for high-temperature TE applications, possess a defected Th_3P_4 structure type due to the valence imbalance of stoichiometric La_3Te_4.[14–17] The high TE performance of $La_{3-x}Te_4$ partly stems from synergistic effects of light and heavy bands leading to overall advantageous electrical transport properties,[18] as well as enhanced phonon scattering from La vacancies.[19] Similar materials, such as $Pr_{3-x}Te_4$,[20,21] $Nd_{3-x}Te_4$,[22] and $La_{3-x}S_4$[23,24] also exhibit low κ and high TE performance, likely due to the high degree of phonon scattering from the cation vacancies. Inspired by this chemical space of materials, the valence-balanced Sc_2Te_3 was synthesized and found to have $\kappa < 2$ W/mK.[25] Due to the prevalence of rare-earth chalcogenide TE materials, it is, therefore, natural to ask if there are other potentially high-performing TE materials within this chemical space.

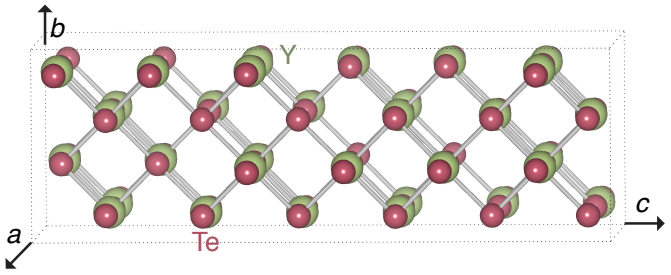

Fig. 1 Rocksalt-like orthorhombic crystal structure of Y_2Te_3 (space group $Fddd$, no. 70). A third of the atomic sites on the cation sublattice are vacancies that are arranged in an ordered fashion.

Zhu et al. identified Y_2Te_3 as a low-κ_L material with promising TE performance in their preliminary investigations.[10] The orthorhombic crystal structure of Y_2Te_3 (space group $Fddd$, Figure 1) can be understood as a rock-salt derived structure with ordered cation vacancies, which is isostructural with the orthorhombic polymorph of Sc_2Te_3.[25] The vacancy-ordered structures of Y_2Te_3 and Sc_2Te_3 are related to that of rhombohedral Sb_2Te_3, as evidenced by their phase transitions in phase-change memory alloys.[26] Specifically, the structural relationship can be understood as a gathering of the ordered vacancies in the orthorhombic structures to form a van der Waals gaps in the rhombohedral Sb_2Te_3 structure, similar to the phase transition mechanism of $Ge_2Sb_2Te_5$.[27,28] Therefore, it is not surprising that layered structures such as Sb_2Te_3 and Bi_2Te_3,,[29] which are derived from rocksalt like structures, as well as $Ge_2Sb_2Te_5$,[30] are well-known TE materials.

Besides the preliminary studies undertaken by Zhu et al.,[10] relatively little is known about the fundamental TE transport properties and doping characteristics of Y_2Te_3. The ordered vacancies in

[a]Northwestern University, Evanston, IL 60208.
[b]Thermal Energy Conversion Materials Group, Jet Propulsion Laboratory/California Institue of Technology, Pasadena, CA 91109.
[c]Colorado School of Mines, Golden, CO 80401.
*E-mail: MichaelToriyama2024@u.northwestern.edu, pgorai@mines.edu
† Electronic supplementary information available.

the Y_2Te_3 structure likely promotes defect scattering of phonons as well as softens the lattice,[31] both of which contribute to the lowering of κ_L. The TE performance of Y_2Te_3 was found to be comparable to $La_{3-x}Te_4$ and $Yb_{14}MnSb_{11}$, reaching a $zT \sim 0.8$ at 900 K when doped/alloyed with Bi.[10] In their study, Zhu et al. acknowledged the anomalous n-type doping with Bi^{3+}, which is expected to isoelectronically substitute Y^{3+}.[10] As such, there are open questions about the transport properties and doping behavior of orthorhombic Y_2Te_3.

To answer some of these questions and to guide future experimental studies, we perform first-principles calculations to investigate the electronic structure, transport properties and doping behavior of Y_2Te_3. We find that there are multiple low-lying and dispersive conduction band (CB) valleys that contribute to high CB degeneracy with the possibility of further enhancement through band convergence. Combined with a low κ_L, Y_2Te_3 has a promising n-type quality factor and therefore, we focus on the n-type doping and TE performance in this study. Our first-principles defect calculations reveal that Y_2Te_3 can be degenerately doped n-type with halogens under Y-rich growth conditions.

2 Results and Discussion

The calculated band structure of Y_2Te_3 along high-symmetry k-point paths is shown in Figure 2(a). The high-symmetry k-points are determined using a methodology developed by Setyawan and Curtarolo.[32,33] The presence of Te-p states at the valence band edge (Figure S1) leads to a triply degenerate valence band maximum (VBM) at the Γ point. On the other hand, the conduction band edge contains multiple low-lying valleys that are mainly composed of Y-d derived states. We find that the conduction band minimum (CBM) is located at the Y-point yielding an indirect band gap of $E_g = 1.78$ eV. Additional band valleys exist at Γ (+0.003 eV), between X and A (+0.115 eV), and at X (+0.180 eV). The corresponding Fermi surface of Y_2Te_3, calculated at an isosurface 0.15 eV above the CBM, is shown in Figure 2(b). The two carrier pockets at Y, along with pockets at Γ and between X and A, together yield a CB degeneracy of $N_v = 4$.

The optimized TE performance can be assessed by calculating

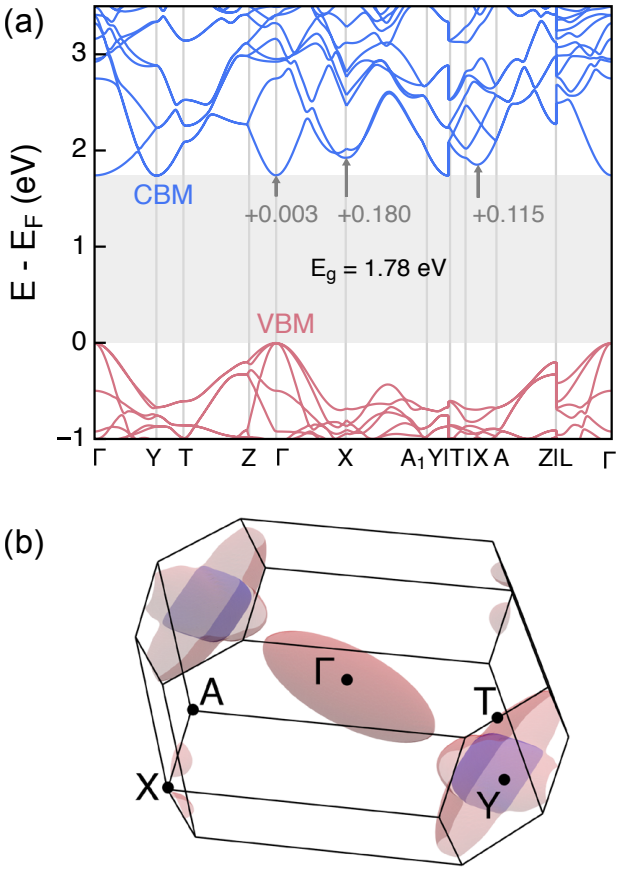

Fig. 2 (a) Band structure of orthorhombic Y_2Te_3 calculated along special k-point paths of the Brillouin zone. Y_2Te_3 has an indirect band gap E_g of 1.78 eV while the direct gap at Γ is only 0.003 eV larger. There are additional low-lying conduction band valleys along X-A and at X, which are above the conduction band minimum (CBM) by 0.115 eV and 0.180 eV, respectively. (b) Fermi surface at 0.15 eV above the CBM. Two carrier pockets exist at Y as shown with two different colors.

the material quality factor β, which is given by

$$\beta \propto \frac{\mu_0 {m^*_{\mathrm{DOS}}}^{3/2}}{\kappa_L} T^{5/2} \quad (1)$$

where μ_0 is the intrinsic carrier mobility, m^*_{DOS} is the density-of-states effective mass, and κ_L is the lattice thermal conductivity. We calculate μ_0 and κ_L at 300K using parameterized semi-empirical models, where the model inputs are obtained from density functional theory (DFT) calculations. The details of these models and computational methodology to calculate the input parameters are documented in Refs. 34 and 35. We estimate the room-temperature κ_L in single crystals to be 2.96 W/mK, which is higher than the experimentally measured value of 1.9 W/mK (at 300 K)[10] in polycrystalline samples where grain boundary scattering lowers κ_L. For consistency, we use our calculated κ_L to evaluate β. Additionally, we estimate the room-temperature mobilities of electrons and holes to be 62 and 20 cm^2/Vs, respectively (Table 1). The mobility computed with the semi-empirical model provides an estimate of the intrinsic phonon scattering-limited mobility and therefore should be treated as an upper limit. Addi-

Table 1 Computed electronic structure parameters, transport and thermoelectric properties of p- and n-type Y_2Te_3. N_V is the valence (p-type) and conduction (n-type) band degeneracy, m^*_{DOS} is DOS effective mass, μ_0 the intrinsic carrier mobility (300 K), κ_L the lattice thermal conductivity (300 K), and $\beta/\beta_{\mathrm{PbTe}}$ is the quality factor, normalized to that of PbTe.

Y_2Te_3	N_V	m^*_{DOS} (m_e)	μ_0 (cm^2/Vs)	κ_L W/mK	$\beta/\beta_{\mathrm{PbTe}}$
p-type	3	0.812	20	2.96	0.59
n-type	4	0.467	62	2.96	1.22

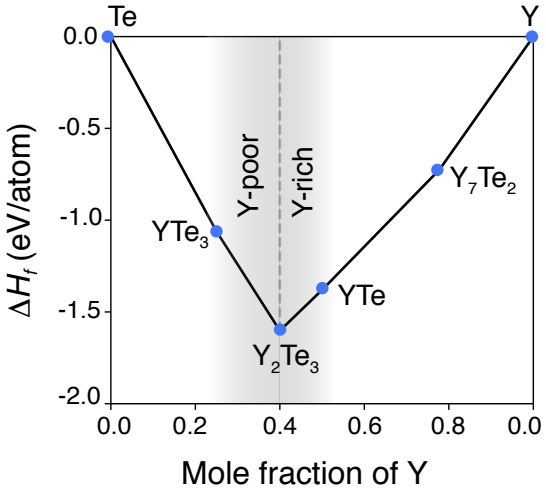

Fig. 3 Phase diagram showing the convex hull formed by the stable competing phases in the binary Y-Te chemical space. The two-phase equilibrium with YTe(YTe_3) sets the most Y-rich(Y-poor) thermodynamic conditions under which Y_2Te_3 is stable despite being off-stoichiometric.

tional sources of scattering such as ionized impurities in heavily-doped semiconductors will reduce the carrier mobility.[36]

Larger β values signify higher optimized TE performance. We find that Y_2Te_3 has a superior n-type quality factor (β_n) of 1.2 (relative to PbTe) compared to its p-type value of 0.6 (Table 1). The larger β_n of Y_2Te_3 is attributed to the high CB valley degeneracy ($N_v = 4$) and low band effective mass m_b^* (0.19 m_e). In the absence of significant intervalley carrier scattering, these conditions are suitable to realize high n-type thermopower without suppressing electron mobility.[37–39]

To realize the predicted n-type TE performance of Y_2Te_3, it must be suitably doped with electrons and the free electron concentration must be tuned to optimize the performance. Whether a material can be optimally doped depends largely on the self-doping behavior of the native defects. The presence of high concentrations of acceptor-like defects will limit n-type doping due to the charge compensation by the holes created by the acceptor defects. Therefore, to probe whether Y_2Te_3 can be doped n-type, we calculate the formation energies of native defects using first-principles calculations. The details of the defect calculations are provided in the Methods section.

Defect formation energy (ΔE_{D^q}) varies with the thermodynamic growth conditions (Eq. 3) of a material, which are determined by the chemical potentials of the constituent elements. In the case of Y_2Te_3, ΔE_{D^q} will depend on the chemical potentials of Y (μ_Y) and Te (μ_{Te}). The elemental chemical potentials μ_i are commonly expressed relative to their chemical potentials at standard conditions such that $\mu_i = \mu_i^0 + \Delta\mu_i$, where $\Delta\mu_i$ quantifies the deviation from standard conditions. The allowable range of $\Delta\mu_i$ is dictated by the thermodynamic phase stability of the material in the grand potential phase diagram obtained through a convex hull analysis.

Figure 3 shows the convex hull formed by the stable competing phases in the binary Y-Te chemical space. The allowed range of $\Delta\mu_Y$ and $\Delta\mu_{Te}$ for the phase stability is set by the two-phase

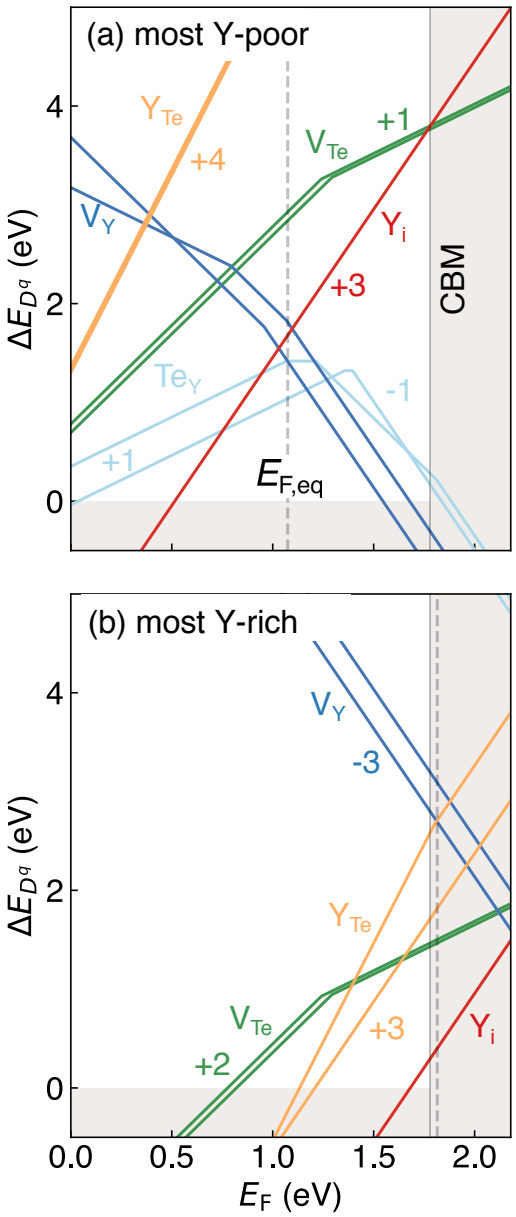

Fig. 4 Formation energy (ΔE_{D^q}) of native defects in Y_2Te_3 under the (a) most Y-poor and (b) most Y-rich conditions within the region of phase stability (Figure 3). The Fermi energy (E_F) is referenced to the valence band maximum (VBM) i.e., E_F = 0 at VBM. The conduction band minimum is labeled CBM. Formation energy of different defect types are plotted in different colors. Multiple lines of the same color represent defects at unique Wyckoff sites. The equilibrium Fermi energy ($E_{F,eq}$), shown as a dashed vertical line, is calculated at 923 K. Y_2Te_3 is insulating under the most Y-poor conditions, but n-type under the most Y-rich conditions due to the low formation energy of donor Y interstitials.

equilibrium of Y_2Te_3 with either YTe_3 or YTe (Table S2). Here, the equilibrium between Y_2Te_3 and YTe_3 is denoted as "most Y-poor" condition since Y_2Te_3 is stable under these thermodynamic conditions despite being compositionally Y-deficient. In a similar fashion, the two-phase equilibrium with YTe is denoted as the "most Y-rich" condition. Since the elemental chemical potentials are different under these two conditions, we present the corresponding native defect formation energies separately in Figures

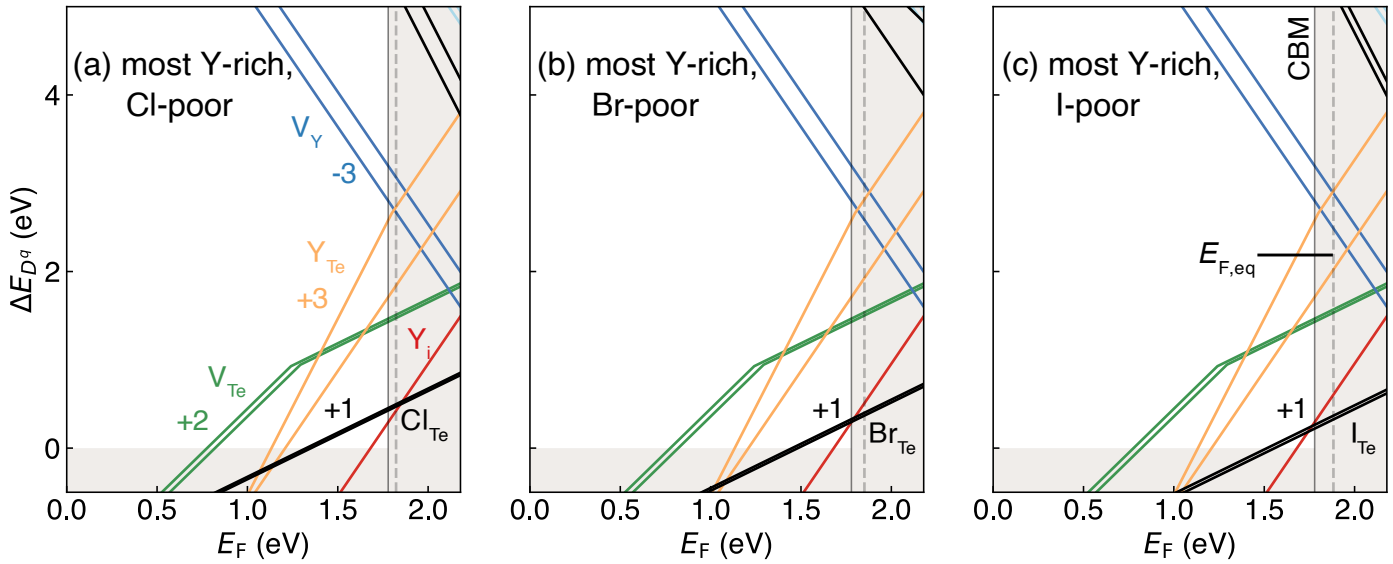

Fig. 5 Formation energy (ΔE_{D^q}) of halogen substitution on the Te site. n-type doping of Y_2Te_3 with (a) Cl, (b) Br, and (c) I, under Y-rich/halogen-poor conditions such that Y_2Te_3 is in equilibrium with YTe and YX_3 (X = Cl, Br, I). The formation energy of native defects (Figure 4b) is shown for reference. The Fermi energy (E_F) is referenced to the valence band maximum (VBM) i.e., E_F = 0 at VBM, and the conduction band minimum is labeled CBM. The equilibrium Fermi energy ($E_{F,eq}$) is calculated at 923 K. Formation energy of different defect types are plotted in different colors. Multiple lines of the same color represent defects at unique Wyckoff sites. Halogens dopants generate high electron concentrations in Y_2Te_3, specifically 1.1×10^{20} cm^{-3} with Cl, 1.5×10^{20} cm^{-3} with Br, and 2.0×10^{20} cm^{-3} with I doping.

4(a) and 4(b).

Under the most Y-poor condition (Figure 4a), Y_2Te_3 is an intrinsic semiconductor with the equilibrium Fermi energy ($E_{F,eq}$) pinned near mid-gap, yielding a net hole concentration of 1.1×10^{16} cm^{-3} at T = 923 K, which is the typical solid-state synthesis temperature. We find that Y_2Te_3 cannot be doped n-type under Y-poor conditions because the low formation energy of acceptor-like cation vacancies (V_Y) indicates that electrons generated by a donor dopant will be charge compensated by the holes produced by V_Y. Similarly, it will be difficult to dope Y_2Te_3 p-type under Y-poor conditions due to the low formation energy of the amphoteric anti-site defect Te_Y. At Fermi energies closer to the valence band, Te_Y acts as a singly-charged donor defect such that holes introduced by an extrinsic p-type dopant will be charge compensated by the electrons from Te_Y. As a result, we predict that it will be difficult to dope Y_2Te_3 either n- or p-type under Y-poor conditions, and will remain an intrinsic semiconductor with low free carrier concentrations.

Our defects calculations suggest that it is possible to dope Y_2Te_3 n-type under Y-rich conditions (Figure 4b) since the formation of acceptor-like native defects (V_Y and Te_Y) is suppressed i.e., acceptor defects have high formation energy. In fact, under Y-rich conditions Y_2Te_3 is found to be self-doped n-type with a free electron concentration of 1.0×10^{20} cm^{-3} at T = 923 K. The relatively high electron concentration is due to the low formation energy of donor-like cation interstitials (Y_i), which reside at the vacancy sites in the ordered-vacancy structure of Y_2Te_3 (Figure S2). In addition, the generated electrons are free conduction electrons and not localized at mid-gap states that require temperature activation. The mid-gap states associated with V_{Te} are occupied when $E_{F,eq}$ is located at ~1.5 eV above the VBM.

Typically, carrier concentrations on the order of $10^{19} - 10^{21}$ cm^{-3} are needed to fully optimize the performance of most thermoelectric materials.[40–42] Therefore, we explore plausible extrinsic dopants to further enhance the electron concentration in n-type Y_2Te_3. We find that halogens (Cl, Br, I) can increase the electron concentration under the most Y-rich and halogen-poor conditions, when Y_2Te_3 is in three-phase equilibrium with YTe and YX_3 (X = Cl, Br, or I). As shown in Figure 5, halogens preferentially substitute on the Te site and create 1-electron shallow donor states. Halogen doping does not introduce mid-gap states, and the generated electrons are therefore available as freely conducting electrons. We predict that the maximum achievable free electron concentrations are 1.1×10^{20} cm^{-3} (Cl doping), 1.5×10^{20} cm^{-3} (Br doping), and 2.0×10^{20} cm^{-3} (I doping). The trend in the electron concentrations can be understood in terms of the halogen solubilities – the lower the formation energy of substitutional X_{Te} defects, the higher is the solubility and concentration of generated electrons. An additional benefit of halogen doping is that the conduction band edge is composed of Y-d states (Figure S1); accordingly, substitution on the Te site does not significantly perturb the conduction band dispersion, and electron mobility will not be severely affected by doping.

The substitution of halogen dopants on the chalcogenide site is a common n-type doping strategy in TE materials e.g., I doping of PbTe,[43] I-doping of Bi_2Te_3,[44] Br-doping of SnSe,[45] and halogen doping to realize n-type BiCuSeO.[46] However, as the defect energetics (and, therefore, the carrier concentrations) are dependent on the thermodynamic equilibrium of the growth conditions,[47] we emphasize the need to dope Y_2Te_3 under Y-rich conditions. In

practice, precise control of the thermodynamic equilibrium (set by the elemental chemical potentials) can be achieved through careful phase boundary mapping experiments,[47,48] wherein the competing phases of a material are detected as impurity phases to gauge the thermodynamic state of the material.

A range of carrier concentrations can be achieved by halogen doping of Y_2Te_3 depending on the thermodynamic equilibrium at different growth conditions (Table S3). For example, while the maximum electron concentration achieved by I doping is 2.0×10^{20} cm^{-3}, it is also possible to have much lower electron concentration e.g., 9.2×10^{16} cm^{-3} when Y_2Te_3 is in equilibrium with YTe_3 and YI_3. This is a direct consequence of two factors: (1) the fundamental dependence of the defect formation energy on the elemental chemical potentials, which are set by the thermodynamic conditions, and (2) charge compensation by acceptor-like defects at certain thermodynamic conditions where they are favorable. As a result, halogen doping of Y_2Te_3 will require careful consideration of the thermodynamic state to rationally optimize *n*-type doping.

Zhu et al. acknowledged the anomalous *n*-type doping with Bi^{3+}, which is expected to isoelectronically substitute Y^{3+}.[10] We try to confirm with defect calculations whether Bi can indeed result in *n*-type character. We consider Bi substitution on Y and Te sites as well as the formation of Bi interstitials. Due to the similarity in their ionic radii, octahedrally-coordinated Bi^{3+} (1.03 Å) is expected to preferentially substitute Y^{3+} (0.9 Å) as opposed to Te^{2-} (2.21 Å).[49] In principle, isovalent Bi substitution on Y should not generate electronic carriers. Bi is known to isovalently substitute Y in bixbyite Y_2O_3, which has similar octahedral coordination as in Y_2Te_3.[50,51] However, we find that the defect energetics (Figure 6) are more nuanced than this simplified treatment.

Our results suggest that isovalent Bi substitution on the Y site (Bi_Y) is preferred under Y-poor/Bi-rich conditions (Figure 6a), which is the expected behavior for Bi doping. In this case, no additional charge carriers (electrons or holes) are created, and the equilibrium Fermi energy ($E_{F,eq}$) is pinned in the gap such that Y_2Te_3 is insulating. Under Y-rich/Bi-poor conditions on the other hand, Bi substitution on Te (Bi_{Te}) becomes energetically favorable. The tendency of Bi to substitute on chalcogen sites is not uncommon; for instance, Bi/Te and Bi/Se anti-site defects are found in Bi_2Te_3 and Bi_2Se_3, respectively,[52] and Bi-doping on the Se site has been able to achieve *n*-type SnSe.[53] Interestingly, in Y_2Te_3, Bi_{Te} is an amphoteric defect i.e., it acts as a donor when E_F is close to the VB and an acceptor when E_F is close to the CB. Under Y-rich/Bi-poor conditions, the equilibrium E_F is closer to the CB where Bi_{Te} is an acceptor defect (Figure 6b). Due to the high formation energy of Bi_{Te}, the dopant does not generate compensating holes significantly, and we therefore predict negligible change in the free electron concentration.

Our results show that Bi doping still maintains the *n*-type character due to donor Y_i, in agreement with the *n*-type character of Bi-doped Y_2Te_3 observed experimentally.[10] However, it is also observed experimentally that increasing the nominal Bi concentration reduces the *n*-type Seebeck coefficient and electrical resistivity, suggesting an increase in the electron concentration.[10] This anomalous effect cannot be explained by a simple site substitution doping mechanism. The Bi-doped Y_2Te_3 samples by Zhu et al.[10] were prepared with high (nominal) concentrations of Bi, which is beyond the dilute doping limit (typically $< 1\%$). Therefore, one plausible explanation for the observed *n*-type character of Bi-doped Y_2Te_3 is that Bi substitution significantly alters the electronic dispersion of both the conduction and valence band edges through substitution on the Y and Te sites, respectively, as the CB and VB edges are primarily composed of Y-*d* and Te-*p* orbitals, respectively (Figure S1). In particular, the perturbation of the CB edge may induce convergence of the multiple low-lying

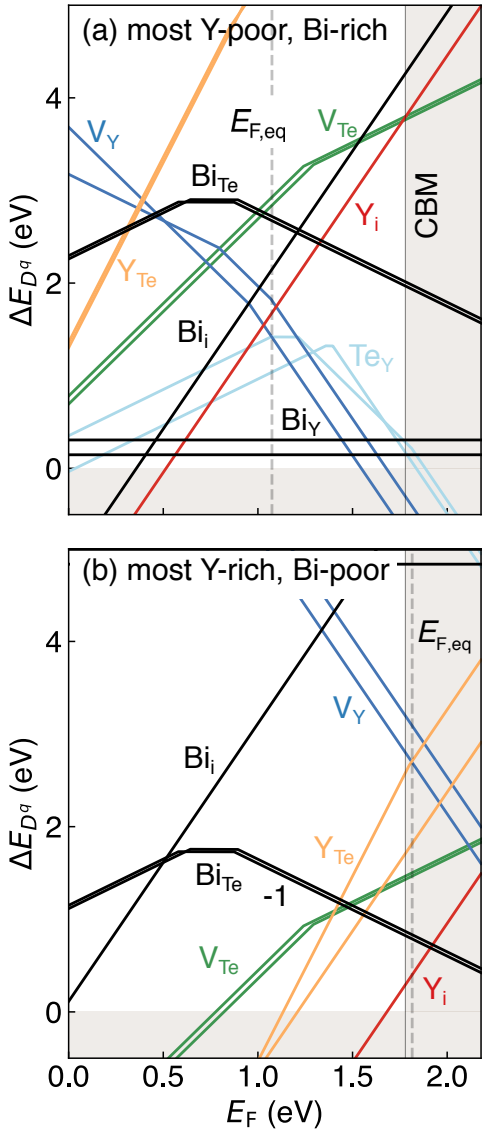

Fig. 6 Formation energy (ΔE_{D^q}) of point defects in Bi-doped Y_2Te_3 under (a) Y-poor (equilibrium with YTe_3, Bi_2Te_3), and (b) Y-rich conditions (equilibrium with YTe, Bi_2Te_3). ΔE_{D^q} of native defects (Figure 4b) is shown for reference. The Fermi energy (E_F) is referenced to the valence band maximum (VBM) i.e., E_F = 0 at VBM. Formation energy of different defect types are plotted in different colors. Multiple lines of the same color represent defects at unique Wyckoff sites. The equilibrium Fermi energy ($E_{F,eq}$) is calculated at 923 K. Bi substitution on the Y site is preferred under Y-poor/Bi-rich conditions while substitution on the Te site under Y-rich/Bi-poor conditions.

valleys (Figure 2a). Secondly, Bi incorporation may form an alloy (rather than a material with dilute doping) with native defect energetics that are different from the undoped Y_2Te_3. Finally, unintentional doping may also lead to confusing results. For example, unintentional H incorporation is responsible for the persistent *n*-type character of wurtzite ZnO and prevent *p*-type doping.[54,55] We therefore attribute the *n*-type character of Bi-doped Y_2Te_3 to either a change in the defect energetics combined with a change in the band edge dispersion or unintentional *n*-type doping not directly related to Bi.

Our results so far suggest that Y_2Te_3 is a promising *n*-type thermoelectric material that can be doped with halogens to enhance the free electron concentration. However, based on the earlier works on rare-earth chalcogenides,[14,20,25] we anticipate synthetic challenges in preparing phase-pure samples. Rare-earth chalcogenides are prone to oxidation and therefore, we computationally assessed the oxidation of Y_2Te_3. In the ternary Y-Te-O phase diagram (Figure S3), Y_2Te_3 shares a tie line with Y_2O_3 forming two three-phase regions where it is in equilibrium either with YTe and Y_2O_3 (Y-rich), or with YTe_3 and Y_2O_3 (Y-poor). We investigate if it is possible to suppress the formation of Y_2O_3 by tuning the oxygen partial pressure (p_{O_2}). The oxygen partial pressure is related to the O_2 chemical potential ($\Delta\mu_{O_2} \equiv 2\Delta\mu_O$, where $\Delta\mu_O$ is the elemental oxygen chemical potential), as

$$p_{O_2} = p^0_{O_2} \exp\left(\frac{\Delta\mu_{O_2}}{k_B T}\right) \quad (2)$$

where k_B is the Boltzmann constant and $p^0_{O_2}$ is the partial pressure under standard conditions i.e., $p^0_{O_2} = 1$ atm. In order to suppress the formation of Y_2O_3 at a given temperature (T), $\Delta\mu_O$ should be lower than the value fixed by the three-phase equilibrium regions. Our analysis shows that, at 1000 K, p_{O_2} must be lower than at least 1.1×10^{-38} atm (Y-poor condition). Such low oxygen partial pressure is currently not achievable even in ultra-high vacuum systems (10^{-13} atm), suggesting oxidation of Y_2Te_3 is imminent. However, the above analysis assumes thermodynamic equilibrium, whereas oxidation is often kinetics and diffusion-limited. It is possible that surface oxidation will protect the bulk from further oxidation, as is observed in other chalcogenide-based thermoelectric materials e.g., SnSe[56,57] and Sc_2Te_3.[25] Therefore, we recommend that future experimental studies of Y_2Te_3 pay close attention to the presence of oxide inclusions in the bulk, as reproducibility has proven difficult in oxidized rare-earth thermoelectric materials such as $La_{3-x}Te_4$.[14,15]

3 Conclusions

We have computationally assessed the prospect of Y_2Te_3 as a *n*-type TE material. A high conduction band valley degeneracy contributes to the superior *n*-type electronic transport properties, which combined with the low lattice thermal conductivity yields a high TE quality factor. Our defect calculations reveal that Y_2Te_3 is natively *n*-type under Y-rich conditions due to the facile formation of donor cation interstitials. The free electron concentration can be further enhanced through halogen doping on the Te site, with I being the most effective dopant. We also clarify through defect calculations that the reported *n*-type character of Bi-doped Y_2Te_3 is not a direct consequence of electron generation from Bi substitution, and further studies are necessary to resolve the unusual experimental observation. We propose that halogens are "better" *n*-type dopants because they preferentially substitute on the Te site and are likely to not perturb the conduction band electronic dispersion, which is dominated by Y-*d* states.

CRediT Statement

Michael Toriyama: Conceptualization, Investigation, Data Curation, Writing (Original Draft), Writing (Editing). **Dean Cheikh**: Investigation, Data Curation, Writing (Editing). **Sabah K. Bux**: Writing (Editing), Supervision. **G. Jeffrey Snyder**: Investigation, Writing (Editing), Supervision. **Prashun Gorai**: Conceptualization, Investigation, Data Curation, Writing (Editing), Supervision, Project Administration.

Acknowledgements

We thank Jiaxing Qu for assistance in analyzing the defect calculations. M.Y.T. is funded by the United States Department of Energy through the Computational Science Graduate Fellowship (DOE CSGF) under grant number DE-SC0020347. P.G. acknowledges support from NSF through award DMR-2102409. The research was performed using computational resources sponsored by the Department of Energy's Office of Energy Efficiency and Renewable Energy and located at the NREL. D.C. and S.K.B. were supported by the NASA Science Missions Directorate under the Radioisotope Power Systems Program's Technology Management Task. GJS acknowledges award 70NANB19H005 from U.S. Department of Commerce, National Institute of Standards and Technology as part of the Center for Hierarchical Materials Design (CHiMaD).

Conflicts of interest

There are no conflicts to declare.

Computational Methods

First-principles density functional theory (DFT) calculations were performed using the Vienna Ab initio Simulation Package (VASP).[58,59] The generalized gradient approximation of Perdew-Burke-Ernzerhof (PBE) was used as the exchange correlation functional.[60] The core and valence electrons were treated with the projector-augmented wave (PAW) method.[61,62] A plane-wave energy cutoff of 340 eV was used, and a Hubbard on-site energy correction of $U = 3$ eV was applied to the Y *d* orbitals.[63,64]

The electronic structure of Y_2Te_3 was calculated from the charge density of the fully-relaxed structure using the tetrahedron method for *k*-point integration and a Γ-centered $8 \times 8 \times 4$ *k*-point mesh.[65] It is well-known that the PBE functional underestimates the band gap of semiconductors and insulators, which directly affects the defect formation energy and resulting charge carrier concentrations. We address the band gap underestimation by shifting the band edge positions based on GW quasiparticle energy calculations,.[66] Due to the presence of Te, we also included band edge shifts due to relativistic spin-orbit coupling effects.[46] The two band edge shifts together result in valence (conduction)

band shifts of -0.511 (+0.490) eV relative to the PBE band edges, yielding a band gap of 1.78 eV.

Point defect calculations were performed using the standard supercell approach.[67–69] A $2\times2\times1$ supercell of Y_2Te_3 containing 80 atoms was considered. The pylada-defects software was used to automate the point defect calculations.[70] Vacancies and anti-site defects in charge states ranging between $q=-3$ and $q=+3$ were considered. Additional charge states were considered where necessary e.g., Y_{Te} in $q=+4$. The ion positions in defect supercells were relaxed using a $4\times4\times4$ Γ-centered k-point mesh. The formation energy ($\Delta E_{D,q}$) of a point defect D in charge state q was calculated according to the equation

$$\Delta E_{D,q} = E_{D,q} - E_{\text{host}} - \sum_i n_i\mu_i + qE_{\text{F}} + E_{\text{corr}} \tag{3}$$

where $E_{D,q}$ and E_{host} are the total energies of the supercell with and without the defect, respectively, and E_{F} is the Fermi energy. n_i is the number of atoms of element i added ($n_i>0$) or removed ($n_i<0$) to create defect D. The elemental chemical potentials μ_i are expressed relative to the reference state chemical potentials (μ_i^0) such that $\mu_i=\mu_i^0+\Delta\mu_i$, where $\Delta\mu_i$ is the deviation from the reference state. The reference state chemical potential μ_i^0 of each element was determined by fitting to a set of experimentally-measured formation enthalpies of several compounds under standard conditions.[71] The fitted elemental reference energies for each element considered in this study are listed in Table S1. The values of $\Delta\mu_Y$ and $\Delta\mu_{Te}$ are bounded by the condition of phase stability of Y_2Te_3. Mathematically, $\Delta\mu_Y$ and $\Delta\mu_{Te}$ must satisfy the equation $2\Delta\mu_Y+3\Delta\mu_{Te}=\Delta H_f^{Y_2Te_3}$, where $\Delta H_f^{Y_2Te_3}$ is the formation enthalpy of Y_2Te_3. Additionally, $\Delta\mu_Y$ and $\Delta\mu_{Te}$ must also satisfy the condition that the competing phases (YTe, YTe_3, Y_7Te_2) are unstable.

Corrections to the defect formation energy (E_{corr}) arising from finite-size effects were calculated following the methodology of Lany and Zunger.[69] Finite-size corrections are applied to address: (i) misalignment of the average electrostatic potential between supercells with and without charged defects, (ii) long-range electrostatic interactions between periodic images of point charges, and (iii) Moss-Burnstein band filling due to shallow defects.[72]

The free charge carrier concentrations were calculated following the charge neutrality condition

$$\sum_{D^q}\left[qN_De^{-\Delta E_{D^q}/k_BT}\right]+p-n=0 \tag{4}$$

where N_D is the site concentration, k_B is the Boltzmann constant, and T is the temperature. We use a typical synthesis temperature of 923 K. The hole (p) and electron (n) concentrations are calculated using the density of states $g(E)$ and the Fermi-Dirac distribution $f(E)$ as

$$p=\int_{-\infty}^{\text{VBM}} g(E)\,[1-f(E)]\,dE \tag{5}$$

$$n=\int_{\text{CBM}}^{\infty} g(E)f(E)dE \tag{6}$$

The density of states was calculated using a $8\times8\times4$ k-point grid using the tetrahedron integration scheme.[73] The free carrier concentration is the net carrier concentration i.e., $|n-p|$.

References

1 G. J. Snyder and E. S. Toberer, *Nat. Mater.*, 2008, **7**, 105.
2 J. Carrete, W. Li, N. Mingo, S. Wang and S. Curtarolo, *Phys. Rev. X*, 2014, **4**, 011019.
3 J. Carrete, N. Mingo, S. Wang and S. Curtarolo, *Adv. Funct. Mater.*, 2014, **24**, 7427.
4 A. Seko, A. Togo, H. Hayashi, K. Tsuda, L. Chaput and I. Tanaka, *Phys. Rev. Lett.*, 2015, **115**, 205901.
5 M. W. Gaultois, A. O. Oliynyk, A. Mar, T. D. Sparks, G. J. Mulholland and B. Meredig, *APL Mater.*, 2016, **4**, 053213.
6 K. F. Garrity, *Phys. Rev. B*, 2016, **94**, 045122.
7 J.-H. Pöhls, A. Faghaninia, G. Petretto, U. Aydemir, F. Ricci, G. Li, M. Wood, S. Ohno, G. Hautier, G. J. Snyder, G.-M. Rignanese, A. Jain and M. A. White, *J. Mater. Chem. C*, 2017, **5**, 12441.
8 X. Wang, S. Zeng, Z. Wang and J. Ni, *J. Phys. Chem. C*, 2020, **124**, 8488.
9 K. Pal, Y. Xia, J. Shen, J. He, Y. Luo, M. G. Kanatzidis and C. Wolverton, *npj Comput. Mater.*, 2021, **7**, 1.
10 T. Zhu, R. He, S. Gong, T. Xie, P. Gorai, K. Nielsch and J. C. Grossman, *Energ. Environ. Sci.*, 2021, **14**, 3559.
11 R. Vickery and H. Muir, *Adv. Energy Conversion*, 1961, **1**, 179.
12 C. Wood, *Rep. Prog. Phys.*, 1988, **51**, 459.
13 G. Mahan and J. Sofo, *P. Natl. A. Sci.*, 1996, **93**, 7436.
14 A. F. May, J.-P. Fleurial and G. J. Snyder, *Phys. Rev. B*, 2008, **78**, 125205.
15 A. May, G. J. Snyder and J.-P. Fleurial, AIP Conf. Proc., 2008, p. 672.
16 A. F. May, J.-P. Fleurial and G. J. Snyder, *Chem. Mater.*, 2010, **22**, 2995.
17 J. M. Ma, S. M. Clarke, W. G. Zeier, T. Vo, P. Von Allmen, G. J. Snyder, R. B. Kaner, J.-P. Fleurial and S. K. Bux, *J. Mater. Chem. C*, 2015, **3**, 10459.
18 A. F. May, D. J. Singh and G. J. Snyder, *Phys. Rev. B*, 2009, **79**, 153101.
19 O. Delaire, A. F. May, M. A. McGuire, W. D. Porter, M. S. Lucas, M. B. Stone, D. L. Abernathy, V. Ravi, S. Firdosy and G. J. Snyder, *Phys. Rev. B*, 2009, **80**, 184302.
20 D. Cheikh, B. E. Hogan, T. Vo, P. Von Allmen, K. Lee, D. M. Smiadak, A. Zevalkink, B. S. Dunn, J.-P. Fleurial and S. K. Bux, *Joule*, 2018, **2**, 698.
21 M. G. Kanatzidis, *Joule*, 2018, **2**, 583.
22 S. J. Gomez, D. Cheikh, T. Vo, P. Von Allmen, K. Lee, M. Wood, G. J. Snyder, B. S. Dunn, J.-P. Fleurial and S. K. Bux, *Chem. Mater.*, 2019, **31**, 4460.
23 C. Wood, A. Lockwood, J. Parker, A. Zoltan, D. Zoltan, L. Danielson and V. Raag, *J. Appl. Phys.*, 1985, **58**, 1542.
24 S. Katsuyama, Y. Tanaka, H. Hashimoto, K. Majima and H. Nagai, *J. Appl. Phys.*, 1997, **82**, 5513.
25 D. Cheikh, K. Lee, W. Peng, A. Zevalkink, J.-P. Fleurial and

S. K. Bux, *Materials*, 2019, **12**, 734.
26 G. M. Zewdie, Y. Zhou, L. Sun, F. Rao, V. L. Deringer, R. Mazzarello and W. Zhang, *Chem. Mater.*, 2019, **31**, 4008.
27 A. Lotnyk, S. Bernütz, X. Sun, U. Ross, M. Ehrhardt and B. Rauschenbach, *Acta Mater.*, 2016, **105**, 1.
28 Z. Song, S. Song, M. Zhu, L. Wu, K. Ren, W. Song and S. Feng, *Sci. China Inf. Sci.*, 2018, **61**, 1.
29 I. T. Witting, T. C. Chasapis, F. Ricci, M. Peters, N. A. Heinz, G. Hautier and G. J. Snyder, *Adv. Electron. Mater.*, 2019, **5**, 1800904.
30 P. Hu, T.-R. Wei, P. Qiu, Y. Cao, J. Yang, X. Shi and L. Chen, *ACS Appl. Mater. Inter.*, 2019, **11**, 34046.
31 T. J. Slade, K. Pal, J. A. Grovogui, T. P. Bailey, J. Male, J. F. Khoury, X. Zhou, D. Y. Chung, G. J. Snyder, C. Uher, V. P. Dravid, C. Wolverton and M. G. Kanatzidis, *J. Am. Chem. Soc.*, 2020, **142**, 12524.
32 W. Setyawan and S. Curtarolo, *Comp. Mater. Sci.*, 2010, **49**, 299.
33 S. Curtarolo, W. Setyawan, G. L. Hart, M. Jahnatek, R. V. Chepulskii, R. H. Taylor, S. Wang, J. Xue, K. Yang, O. Levy, M. J. Mehl, H. J. Stokes, D. O. Demchenko and D. Morgan, *Comp. Mater. Sci.*, 2012, **58**, 218.
34 J. Yan, P. Gorai, B. Ortiz, S. Miller, S. A. Barnett, T. Mason, V. Stevanović and E. S. Toberer, *Energ. Environ. Sci.*, 2015, **8**, 983.
35 S. A. Miller, P. Gorai, B. R. Ortiz, A. Goyal, D. Gao, S. A. Barnett, T. O. Mason, G. J. Snyder, Q. Lv, V. Stevanović and E. S. Toberer, *Chem. Mater.*, 2017, **29**, 2494.
36 Y. Peter and M. Cardona, *Fundamentals of semiconductors: physics and materials properties*, Springer Science & Business Media, 2010.
37 H. Wang, Y. Pei, A. D. LaLonde and G. J. Snyder, *Thermoelectric Nanomaterials*, Springer, 2013, p. 3.
38 P. Norouzzadeh and D. Vashaee, *Sci. Rep.*, 2016, **6**, 1.
39 J. Xin, Y. Tang, Y. Liu, X. Zhao, H. Pan and T. Zhu, *npj Quant. Mater.*, 2018, **3**, 1.
40 A. D. LaLonde, Y. Pei, H. Wang and G. J. Snyder, *Mater. Today*, 2011, **14**, 526.
41 M. Zhou, Z. M. Gibbs, H. Wang, Y. Han, C. Xin, L. Li and G. J. Snyder, *Phys. Chem. Chem. Phys.*, 2014, **16**, 20741.
42 C. J. Perez, M. Wood, F. Ricci, G. Yu, T. Vo, S. K. Bux, G. Hautier, G.-M. Rignanese, G. J. Snyder and S. M. Kauzlarich, *Sci. Adv.*, 2021, **7**, eabe9439.
43 J. Male, M. T. Agne, A. Goyal, S. Anand, I. T. Witting, V. Stevanović and G. J. Snyder, *Mater. Horiz.*, 2019, **6**, 1444.
44 F. Wu, W. Wang, X. Hu and M. Tang, *Prog. Nat. Sci.-Mater.*, 2017, **27**, 203.
45 C. Chang, M. Wu, D. He, Y. Pei, C.-F. Wu, X. Wu, H. Yu, F. Zhu, K. Wang, Y. Chen, L. Huang, J.-F. Li, J. He and L.-D. Zhao, *Science*, 2018, **360**, 778.
46 M. Y. Toriyama, J. Qu, G. J. Snyder and P. Gorai, *J. Mater. Chem. A*, 2021, **9**, 20685.
47 S. Ohno, K. Imasato, S. Anand, H. Tamaki, S. D. Kang, P. Gorai, H. K. Sato, E. S. Toberer, T. Kanno and G. J. Snyder, *Joule*, 2018, **2**, 141.
48 M. Wood, M. Y. Toriyama, S. Dugar, J. Male, S. Anand, V. Stevanović and G. J. Snyder, *Adv. Energy Mater.*, 2021, **11**, 2100181.
49 R. D. Shannon, *Acta Crystall. A-Crys.*, 1976, **32**, 751.
50 H. Choi, S. H. Cho, S. Khan, K.-R. Lee and S. Kim, *J. Mater. Chem. C*, 2014, **2**, 6017.
51 S.-I. Park, S.-I. Kim, S. K. Chang and Y.-H. Kim, *Thin Solid Films*, 2016, **600**, 83.
52 D. Scanlon, P. King, R. P. Singh, A. De La Torre, S. M. Walker, G. Balakrishnan, F. Baumberger and C. Catlow, *Adv. Mater.*, 2012, **24**, 2154.
53 A. T. Duong, V. Q. Nguyen, G. Duvjir, V. T. Duong, S. Kwon, J. Y. Song, J. K. Lee, J. E. Lee, S. Park, T. Min, J. Lee, J. Kim and S. Cho, *Nat. Commun.*, 2016, **7**, 1.
54 C. G. Van de Walle, *Phys. Rev. Lett.*, 2000, **85**, 1012.
55 A. Janotti and C. G. Van de Walle, *Nat. Mater.*, 2007, **6**, 44.
56 Y. Li, B. He, J. P. Heremans and J.-C. Zhao, *J. Alloy. Compd.*, 2016, **669**, 224.
57 C. Zhou, Y. K. Lee, Y. Yu, S. Byun, Z.-Z. Luo, H. Lee, B. Ge, Y.-L. Lee, X. Chen, J. Y. Lee, O. Cojocaru-Mirédin, H. Chang, J. Im, S.-P. Cho, M. Wuttig, V. P. Dravid, M. G. Kanatzidis and I. Chung, *Nat. Mater.*, 2021, **20**, 1378.
58 G. Kresse and J. Furthmüller, *Comp. Mater. Sci.*, 1996, **6**, 15.
59 G. Kresse and J. Furthmüller, *Phys. Rev. B*, 1996, **54**, 11169.
60 J. P. Perdew, K. Burke and M. Ernzerhof, *Phys. Rev. Lett.*, 1996, **77**, 3865.
61 P. E. Blöchl, *Phys. Rev. B*, 1994, **50**, 17953.
62 G. Kresse and D. Joubert, *Phys. Rev. B*, 1999, **59**, 1758.
63 S. Dudarev, G. Botton, S. Savrasov, C. Humphreys and A. Sutton, *Phys. Rev. B*, 1998, **57**, 1505.
64 P. Gorai, E. S. Toberer and V. Stevanović, *Phys. Chem. Chem. Phys.*, 2016, **18**, 31777.
65 H. J. Monkhorst and J. D. Pack, *Phys. Rev. B*, 1976, **13**, 5188.
66 H. Peng, D. O. Scanlon, V. Stevanovic, J. Vidal, G. W. Watson and S. Lany, *Phys. Rev. B*, 2013, **88**, 115201.
67 C. Freysoldt, B. Grabowski, T. Hickel, J. Neugebauer, G. Kresse, A. Janotti and C. G. Van de Walle, *Rev. Mod. Phys.*, 2014, **86**, 253.
68 S. Lany and A. Zunger, *Model. Simul. Mater. Sc.*, 2009, **17**, 084002.
69 S. Lany and A. Zunger, *Phys. Rev. B*, 2008, **78**, 235104.
70 A. Goyal, P. Gorai, H. Peng, S. Lany and V. Stevanović, *Comp. Mater. Sci.*, 2017, **130**, 1.
71 V. Stevanović, S. Lany, X. Zhang and A. Zunger, *Phys. Rev. B*, 2012, **85**, 115104.
72 E. Burstein, *Phys. Rev.*, 1954, **93**, 632.
73 P. E. Blöchl, O. Jepsen and O. K. Andersen, *Phys. Rev. B*, 1994, **49**, 16223.

— Supplementary Information —

Y_2Te_3: A New n-type Thermoelectric Material

Michael Y. Toriyama,*,† Dean Cheikh,‡ Sabah K. Bux,‡ G. Jeffrey Snyder,† and Prashun Gorai*,¶

†*Materials Science and Engineering, Northwestern University, Evanston, IL 60208, USA.*

‡*Jet Propulsion Laboratory, Pasadena, CA 91109, USA.*

¶*Metallurgical and Materials Engineeering, Colorado School of Mines, Golden, CO 80401, USA.*

E-mail: MichaelToriyama2024@u.northwestern.edu; pgorai@mines.edu

Electronic Structure of Y_2Te_3

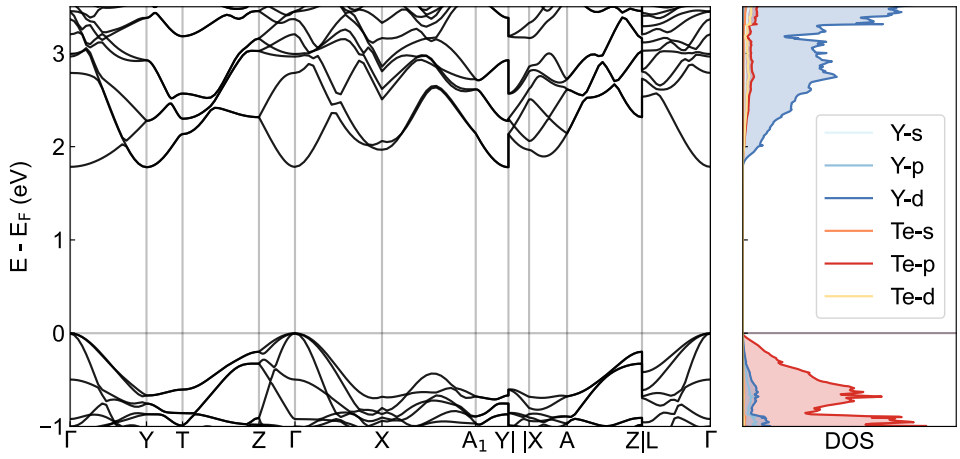

Figure S1: Atomic orbital contributions to the electronic structure of Y_2Te_3. Te-*p* orbitals dominate the valence band edge, while the conduction band edge is primarily composed of Y-*d* orbitals.

Structure of Y Interstitials in Y_2Te_3

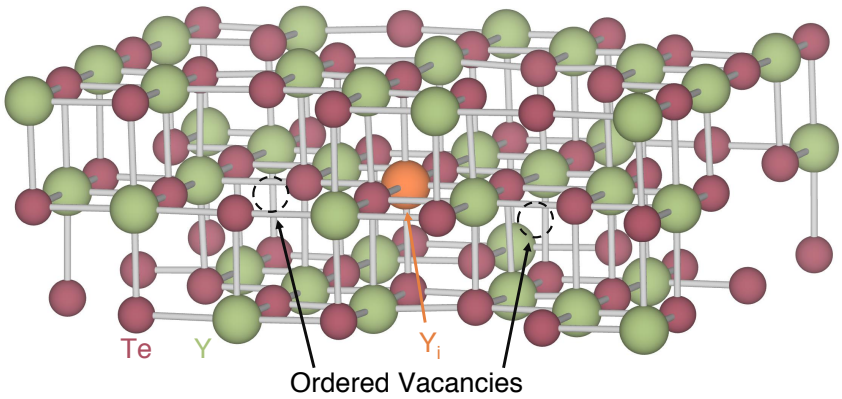

Figure S2: Structure of Y interstitials in Y_2Te_3. In the rocksalt-like orthorhombic crystal structure of Y_2Te_3 (space group *Fddd*, no. 70), a third of the atomic sites on the cation sublattice are vacancies that are arranged in an ordered fashion. Y interstitials occupy these cation vacancy sites in the structure.

Reference Elemental Chemical Potentials

Element	μ^0 (eV)
Y	-5.31
Te	-3.02
Bi	-4.18
Cl	-1.51
Br	-1.28
I	-1.32
O	-4.76

Table S1: Elemental reference chemical potentials μ^0, fitted to experimental formation enthalpies.[1,2] The GGA+U functional is used to calculate the total energy of the compounds used in the fitting.

Phase Equilibria of Y_2Te_3

Equilibrium Phases	$\Delta\mu_Y$	$\Delta\mu_{Te}$	$n-p$ (cm^{-3})
YTe	-0.267	-2.492	1.03×10^{20}
YTe_3	-3.767	-0.159	1.10×10^{16}

Table S2: Chemical potentials $\Delta\mu_i$ (in eV) in the Y-rich and Y-poor equilibrium phase regions of Y_2Te_3. The corresponding free electron concentration in each phase region calculated at 923 K is listed. n (p) denotes electron(hole) concentrations (in cm^{-3}).

Phase Equilibria of Y_2Te_3 With Dopants

Dopant	Equilibrium Phases	$\Delta\mu_Y$	$\Delta\mu_{Te}$	$\Delta\mu_{Dopant}$	$n-p$ (cm^{-3})
Cl	YTe, YCl_3	-0.267	-2.492	-3.391	1.11×10^{20}
	YTe_3, YCl_3	-3.767	-0.159	-2.224	3.99×10^{16}
Br	YTe, YBr_3	-0.267	-2.492	-2.923	1.49×10^{20}
	YTe_3, YBr_3	-3.767	-0.159	-1.757	6.98×10^{16}
I	YTe, YI_3	-0.267	-2.492	-2.126	2.04×10^{20}
	YTe_3, YI_3	-3.767	-0.159	-0.959	9.17×10^{16}
Bi	YTe, Bi_2Te_3	-0.267	-2.492	-1.572	1.03×10^{20}
	YTe_3, Bi_2Te_3	-3.767	-0.159	-0.384	1.10×10^{16}

Table S3: Chemical potentials $\Delta\mu_i$ (in eV) in all phase regions of the ternary Y-Te-dopant phase space that are in equilibrium with Y_2Te_3. The corresponding free electron concentration in each phase region calculated at 923 K is listed. n (p) denotes electron(hole) concentrations (in cm^{-3}).

Y-Te-O Ternary Phase Diagram

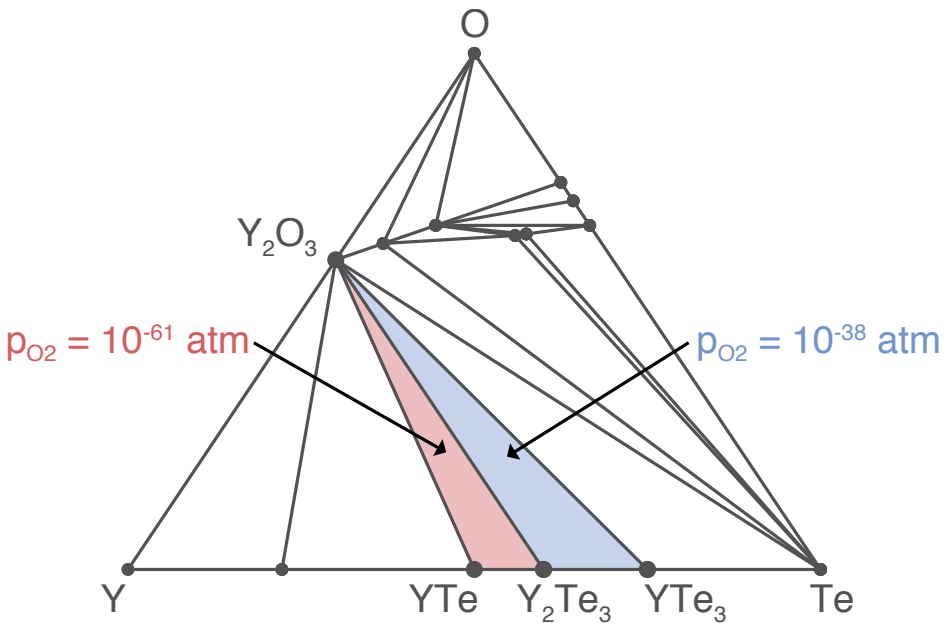

Figure S3: Y-Te-O ternary phase diagram, which shows that Y_2Te_3 shares a tie lie with Y_2O_3. The oxygen partial pressures (p_{O_2}) are shown for the two three-phase equilibrium regions of Y_2Te_3 at 1000 K, assuming a standard reference state of $p^0_{O_2} = 1$ atm.

References

(1) Lany, S. Semiconductor thermochemistry in density functional calculations. *Phys. Rev. B* **2008**, *78*, 245207.

(2) Stevanović, V.; Lany, S.; Zhang, X.; Zunger, A. Correcting density functional theory for accurate predictions of compound enthalpies of formation: Fitted elemental-phase reference energies. *Phys. Rev. B* **2012**, *85*, 115104.